Title: Full-length structure and heme binding in the transcriptional regulator HcpR

B. Ross Belvin[1], Faik N. Musayev[2,3], Carlos Escalante[4], Janina P. Lewis[1,5,6]*

[1]The Philips Institute for Oral Health Research, Virginia Commonwealth University, Richmond, VA 23298

[2]Department of Medicinal Chemistry, Virginia Commonwealth University, Richmond, VA 23298

[3]The Center for Drug Discovery, Virginia Commonwealth University, Richmond, VA 23298

[4]Department of Physiology and Biophysics, Virginia Commonwealth University, Richmond, VA 23298

[5]Department of Biochemistry and Molecular Biology, Virginia Commonwealth University, Richmond, VA 23298

[6]Department of Microbiology and Immunology, Virginia Commonwealth University, Richmond, VA 23298

*Correspondence email: jplewis@vcu.edu

Abstract

HcpR is a CRP-family transcriptional regulator found in many Gram-negative anaerobic bacteria. In the perio-pathogen *Porphyromonas gingivalis,* HcpR is crucial for the response to reactive nitrogen species such as nitric oxide (NO). Binding of NO to the heme group of HcpR leads to transcription of the redox enzyme Hcp. However, the molecular mechanisms of heme binding to HcpR remain unknown. In this study we present the 2.3Å structure of the *P. gingivalis* HcpR. Interdomain interactions present in the structure help to form a hydrophobic pocket in the N-terminal sensing domain. A comparison analysis with other CRP-family members reveals that the molecular mechanisms of HcpR-mediated regulation may be distinct from other family members. Using docking studies, we identify a putative heme binding site in the sensing domain. *In vitro* complementation and mutagenesis studies verify Met68 as an important residue in activation of HcpR. Finally, heme binding studies with purified forms of recombinant HcpR support Met68 and His149 residues as important for proper heme coordination in HcpR.

Introduction

HcpR is a sensor-transcriptional regulator of the nitrosative stress response. Found in many Gram-negative anaerobic bacteria, it regulates the expression of *hcp*, an enzyme crucial for survival in response to nitric oxide (NO) and other forms of nitrosative stress [1,2]. HcpR belongs to the cAMP receptor (CRP) family of proteins of which the catabolite gene activator protein (CAP) and the CO sensing protein CooA are also members [3,4]. This large family of proteins sense changes in the intra-cellular environment by binding effector molecules that allosterically activate the protein for DNA

binding [5]. The CRP family contains a significant number of sub-families that have evolved to sense a wide variety of effector molecules and utilize different cofactors [5]. One of these sub-families, the DNR-HcpR group has evolved to sense NO using metal cofactors such as heme and is phylogenetically distinct from other heme containing CAP family members such as CooA [6]. Although not all HcpRs have been demonstrated to bind heme, a growing subset have been characterized as heme binding proteins [7].

HcpR is crucial for the survival of the periodontal pathogen *Porphyromonas gingivalis* [8]. In the periodontal pocket, *P. gingivalis* is exposed to numerous nitrosative stresses, including immune cell derived NO as well as elevated levels of nitrite from saliva [9,10]. Loss of *hcpR* or *hcp* sensitizes the bacteria to physiological concentrations of nitrite and NO and causes decreased survival with host cells and *in vivo* using mouse models [8,11–13]. Previously we have demonstrated that HcpR from *P. gingivalis* can sense nanomolar concentrations of NO and upregulates the expression of *hcp* in response to these stresses [13]. Furthermore, we have shown that binding of HcpR to the *hcp* promoter is dependent on heme [8].

In heme-based sensor proteins, the heme iron complex serves as the binding site for gaseous molecules such as NO, CO, or O_2. Displacement of an axial side chain that coordinates the heme iron is often utilized for allosteric activation of heme proteins [14,15]. In HcpR, the heme exists in a 6-coordinate system in the unbound when no gas is bound; upon addition of NO, this switches to a 5-coordinate system [13]. The capability of NO to displace the proximal side chain is a distinctive facet of the NO-heme interaction that is not typically seen in CO or O_2 heme sensor proteins [15]. The 5-coordinate NO bound heme in NO sensor proteins such as HcpR and DNR distinguishes it from the CO sensor CooA, which is a 6-coordinate system in the CO bound state [16,17]. The different nature of the gas binding properties has implications for the mechanism of NO dependent activation in HcpR.

So far, the identity of the axial side chains in HcpR is not known. Furthermore, the nature of heme binding to HcpR (the location of the exact heme binding pocket) is not understood. Previously we have solved the structure of the sensing domain of HcpR (ΔCHcpR), that lacks the (highly flexible) C-terminal DNA binding domain [8]. While the truncated structure confirms the inclusion of HcpR as CRP-family regulator, information on inter-domain interactions and how this may influence the heme binding nature of the protein was lost. In this study, we present the structure of the full-length HcpR (FL HcpR). Using a docking approach supported by site-directed mutagenesis and heme binding studies, we identify a putative heme-binding site and important residues in heme coordination. A comparison of HcpR with the structures of CooA and CAP reveals a novel mechanism that may control the NO-mediated activation of HcpR.

Materials and Methods

Generation of recombinant proteins

The full length of the HcpR-encoding gene (PG1053) was cloned into the pET21d vector at the *Bam*HI and *Xho*I sites using gene specific primers with complimentary restriction site overhangs. Vector and PCR fragments were cleaved, purified, ligated and then transformed into DH5α *E. coli* for screening. Positive clones were identified and whole plasmid sequencing was subsequently performed to confirm the proper genetic content. The recombinant *hcpR*-pET21

vector was transformed into BL21(DE3) or Lemo21(DE3) cells (New England Biolabs) to enable inducible protein expression.

For recombinant HcpR expression, overnight culture was used to inoculate 1 L of LB broth. Cultures were grown at 37°C with antibiotics (50 ug/mL carbenicillin) and shaking until cultures reached mid-log phase (0.5-0.7 OD600) and expression of HcpR was induced using 1mM IPTG overnight at 37°C. HcpR was affinity purified using Ni-NTA agarose (Qiagen) or TALON Cobalt resin (ThermoFisher). Briefly, cells were lysed using CellLytic B reagent (Millipore-Sigma) and cell supernatant was added to column containing metal affinity resin. Columns were washed with a 50mM $Na_2H_1PO_4$, 300mM NaCl, 20mM imidazole, pH 8.0 buffer. For elution, imidazole concentration was increased to 250mM. For crystallization, HcpR was further purified via gel exclusion chromatography on a Superdex 75 column. Purification of recombinant mutant HcpRs was performed identically to the wildtype HcpR.

For heme reconstitution, purified HcpR was concentrated and desalted into a 25mM Phosphate, 150mM NaCl, 1mM TCEP pH 7.4 buffer using a PD-10 desalting column. A 1.1 molar excess of heme was added to purified HcpR and allowed to incubate overnight. To remove unbound heme, HcpR was dialyzed overnight and/or desalted using a spin column.

Crystallization and structure determination

Freshly prepared HcpR (15.1mg/ml) in 25mM Tris-HCl, 150mM NaCl, 1mM TCEP, pH 7.0 was used to screen for initial crystallization condition using a wide range of commercially available screening kits with the Gryphon crystallization robot (Art Robbins) employing the sitting-drop vapor-diffusion method at 20°C. 0.3µl of protein solution and 0.3 µl of reservoir were mixed to equilibrate against 60µl reservoir solution. Crystals appeared in one week under several conditions (K/Na tartrate, Na formate, Na citrate tribasic and PEG-3350) at pH range 4.6-6.5. We have crystallized high diffraction grade single crystal of wild type HcpR at low pH (4.6). Crystallization condition was 0.1M sodium acetate, pH 4.6 and 1.8M sodium formate. The crystals diffracted up to 2.3Å resolution and belonged to space group P212121 with the unit cell dimensions of a = 106.260, b = 106.303, and c = 116.773Å. Crystals were fished from the drops and cryo-protected by mother liquor varied concentration of glycerol (10-20%). Subsequently, fished crystals were flash-cooled in a cryogenic nitrogen stream. X-ray diffraction data were collected at 100K using Rigaku MicroMax-007 HF X-ray generator and an EIGER R 4M detector. The data was processed with *CrysAlis*^{Pro} 40.64.69a (Rigaku) and the CCP4 suite of programs.

Model building and refinement

The crystal structure was solved with *Phaser* in the *Phenix* software package using the sensing domain of HcpR (PDB entry: 6NP6) as the search model. Auto model building resulted in an initial model of 572 amino-acid residues built with R_{work} 28.21% and R_{free} 31.71%. The structure was refined with the Phenix software along with manual model building using the graphics program Coot. After several cycles of refinement and manual model building positive electron density belonging to the C-terminal domain became visible. It was possible to fit helix-turn-helix motif of DNA binding domain. The structure was refined to 2.3Å resolution with a final R_{work} of 21.57% and R_{free} of 26.47%.

118 **Docking studies**

119 Structural models of the heme group and the FL-HcpR dimer were prepared for docking
120 calculations using the Graphical User Interface AutoDock Tools (ADT). The grid size was set to 40 x
121 40 x 40 xyz points with grid spacings of 0.375 Å and grid center was placed at x= 111.826, y= 42.032,
122 z= 151.488. Other parameters were maintained at the default configuration. The two pqt files were
123 imported into AutoDock Vina tool based on a fixed geometry of HcpR and Heme. The result with the
124 lowest energy of binding (-8.3 kcal/mol) was selected for further analysis in ChimeraX.

125

126 **UV-Vis spectrum studies**

127 The spectrum of heme-reconstituted HcpR was recorded using a Genesys 150 UV-Vis
128 spectrophotometer (ThermoFisher) in a gas tight 1 cm quartz cuvette in 25mM sodium phosphate,
129 150mM NaCl, 1mM TCEP, pH 7.4 buffer. The ferrous form of heme was obtained by adding an
130 excess of sodium dithionite. To obtain anaerobic samples, purified HcpR was incubated in an
131 anaerobic chamber overnight.

132 **Bacterial strains and growth conditions**

133 *P. gingivalis* W83 (strain V2802) was grown and maintained in an atmosphere consisting of
134 80% N2, 10% CO2, and 10% H2 in an anaerobic chamber (Coy Laboratories). The *hcpR* deficient *P.*
135 *gingivalis* (V2807) was derived previously [8]. *P. gingivalis* strains were grown on TSA-blood agar plates
136 (Tryptic Soy Agar, 5% Sheep blood) or in tryptic soy broth (TSB) supplemented with hemin (5 ug/mL)
137 and Vitamin K (1 ug/mL). Plasmid containing strains were maintained on plates or grown in TSB
138 broth containing tetracycline (0.5 ug/mL).

139 **Cloning and site directed mutagenesis of *P. gingivalis hcpR* complement plasmids**

140 The *P. gingivalis hcpR* deficient strain (V2807) was complemented using the pG108 plasmid
141 [18]. A copy of the *hcpR* gene was synthesized downstream of the *ermF* promoter to create a
142 construct that will constitutively express HcpR. The construct was cloned into the pG108 vector at
143 the *Sph*I and *Bam*HI restriction sites to create the pG108-*hcpR* plasmid. Single amino acid mutants
144 were created using the QuikChange II XL site directed mutagenesis kit (Agilent). Primers were
145 designed to introduce mutations at Met68, His149 and L156 to convert them to Ala or a stop-
146 codon. Primers used for this study are listed in supplemental table. Clones generated from
147 mutagenesis were submitted for full plasmid sequencing and positive clones were used to
148 complement the *hcpR* deficient V2807 strain.

149 **Electroporation and complementation of HcpR-deficient *P. gingivalis***

150 Fresh bacterial cultures on blood plates were used to inoculate 5 ml of BHI broth culture
151 overnight at 37°C. The next day, this culture was diluted 1:10 with fresh media and grown to mid-log
152 phase (0.5-0.6 OD_{600}). Cells were harvested by centrifugation at 8000x g for 15 minutes at 4°C,
153 washed in 25mL cold electroporation buffer (10% glycerol, 1mM MgCl2) and suspended in ~250 µL
154 EP buffer. To a pre-chilled 0.2 cm electroporation cuvette, 50 µL of washed cells and 1-2 ug of
155 pG108-*hcpR* plasmid DNA was added. The cuvette was placed in an electroporation chamber and
156 pulsed using settings at 2.5kV, 5msec, 400 Ω on a BioRad Gene Pulser II. Immediately after

electroporation, 500 µL of pre-warmed media was added and cells were grown overnight in the anaerobic chamber. The next day, the bacteria were plated on TSA-blood agar plates supplemented with 0.5ug/mL tetracycline. Colonies that appeared after 5-6 days of incubation were replated and screened for proper genetic content.

Nitrite growth studies

Overnight cultures of plasmid complemented Δ*hcpR P. gingivalis* started from TSA-blood plates were diluted to on OD_{600} of 0.05. These cultures were supplemented with 0 mM, 1mM, or 2mM sodium nitrite and grown overnight anaerobically at 37°C. The next day the $OD6_{600}$ was measured to assess growth of the *P. gingivalis*strains.

qRT-PCR

To test HcpR activity *in vitro, P. gingivalis* V2807 complemented with plasmids containing recombinant *hcpR* were grown to mid-log phase in TSB broth and then exposed to 0.2mM nitrite for 15 minutes. The bacterial cells were harvested, RNA was purified using Zymo Quick-RNA mini-prep kit, treated with DNA-free DNAse kit (ThermoFisher) and cDNA was generated using High-Capacity cDNA reverse transcriptase kit (ThermoFisher). Real time qPCR analysis was performed with a SYBR green based detection system on a Quant Studio 3 thermal cycler. Primers used for qPCR: hcp-F: AAAGCTGTCATCGTCCTGCT ; hcp-R: CGATCAGCGTCCGAATATCT ; Pg16s-F: AGGCGGAATTCGTGGTGTAG ; Pg16s-R: TTTGATACCCACGCCTTCGT

Bioinformatics

Molecular graphics and analyses were performed with UCSF ChimeraX, developed by the Resource for Biocomputing, Visualization, and Informatics at the University of California, San Francisco, with support from National Institutes of Health R01-GM129325 and the Office of Cyber Infrastructure and Computational Biology, National Institute of Allergy and Infectious Diseases [19,20]. ChimeraX was used to superimpose structures, determine distances, and any potential clashes/contracts. AlphaFold 3 was used to model the DNA binding domains in the active form bound to DNA [21]. Sequence alignments were constructed using Clustal Omega [22]. Alignments were portrayed using Jalview [23].

Results

Overview of the structure of full length HcpR

Crystals of the FL-HcpR belong to the space group $P4_12_12$ and diffracted to 2.3 Å. The structure was solved by molecular replacement using the truncated HcpR structure (PDB ID 6NP6). The asymmetric unit contains 2 dimers with chains A, B, C, and D. There was no significant loss of electron density along the backbone of the structure, and all 228 amino acids of the gene CDS are accounted for. In subunits A and C, the uncleaved cloning tail containing polyhistidine and TEV sites can also be observed on the map. The data collection and refinement statistics are summarized in Table 1.

Structurally, each monomer of HcpR comprises an N-terminal ligand sensing domain (SD) and a C-terminal DNA binding domain (DBD). In agreement with our previous work, HcpR forms a ~48 kDa homodimer (Fig 1A). In HcpR, the SD encompasses residues M1-L151 (Figure 1A). The DBD

196 extends from residues L156-E228 and forms a winged helix turn helix motif. The dimerization
197 helices (helix E) of each monomer form a leucine zipper motif along residues P127-L151 with
198 interface interactions between symmetry-related Leu, Ile, and Met residues stabilizing the
199 formation of the homodimer (Fig 1B). The leucine zipper and DBD are connected by residues
200 spanning S152-L156, known as the 'hinge'. This is a metamorphic region that is unfolded in chain A,
201 but forms part of an extended helix E in chain B, spanning residues 127 to 171 (Figure 1C). This
202 hinge property is key to the mechanisms that govern the activation and DNA binding of many CRP
203 family regulators [24].

204 The ligand sensing domain of HcpR is composed of 7 β-sheets and 4 α-helices. The β-
205 sheets form a β-barrel or "jelly roll" like fold typically found in the FNR-CRP family of regulators.
206 According to the standard topology of CRP-family regulators, this region consists of 8 β-sheets
207 organized in an anti-parallel fashion. Consistent with what was observed in the crystal structure of
208 the truncated HcpR, the location of the 6th β-sheet is completely distorted, owing to a proline
209 residue (Pro89) creating an extended loop in the β6- β7 turn with a 1 turn helix. The presence of this
210 extended loop region thereby influences the potential size and location of the ligand binding
211 pocket. Pro89 and the region surrounding it is highly conserved in the HcpRs from *Porphyromonas*
212 and *Prevotella* species (Fig. S1), indicating it may play a pivotal role in the formation of the ligand
213 binding pocket.

214 Superimposing the two HcpR chains identified three structurally dissimilar regions (rmsd
215 2.14 Å). The DNA binding domain of chain B is rotated by almost 166° with respect to that of chain
216 A (Fig. 1D). One subunit is in an 'OFF' state, while the other is in an apparent 'ON' state. The second
217 region is in the position of the flap region, with a rotation of 39.6° between them (Fig. 1E). The
218 difference in conformation is generated by the interaction between the β-hairpin of chain A and the
219 DBD of chain B, particularly an interaction between R226 and main chain carbonyl oxygens from
220 V69 and G70 (Fig. S2). The final region is in the second half of the leucine zipper, where they
221 superimpose, forming a 13.5° angle (Fig. 1E).

222 **Comparison to other CRP-family regulators**

223 A structural comparison with CooA, the only structurally shown heme-binding protein
224 belonging to the CRP family, was carried out to identify the potential heme binding pocket in HcpR
225 (Figure 4). Overall, the secondary structure features and domain architectures are well conserved
226 between the two proteins and they superimpose with a rmsd of 5.45 Å (Fig 2A). In CooA the heme
227 binding pocket is located at the first half of the α-helices forming the leucine zipper. The heme
228 group is coordinated by the N-terminal Pro2 of one subunit and His77 of the second subunit
229 located on the loop connecting β6 and β7 (Fig. 2B). From the superposition, the position of the
230 heme group in HcpR is occupied by the extended loop connecting β6 and β7 which is significantly
231 longer and has a short 1 turn α-helix (Fig. 2B). This extension is also evident in the sequence
232 alignment of HcpR and CooA (Fig. S3). Moreover, in HcpR, no residues are nearby to coordinate
233 with the heme group. Comparison with CAP reveals that the heme and cyclic-AMP binding sites are
234 situated in close but not identical positions (Fig. S4A). In HcpR, the extended loop region once
235 again occupies a similar location, partially occupying the cyclic-AMP binding site in CAP (Fig. S4B).
236 Furthermore, the overall volume of the pocket in CAP is smaller to accommodate the smaller ligand

237 cAMP. Taken together, we conclude that the presence of the long β6-β7 loop suggests that the heme
238 binding pocket in HcpR must be in a different location.

239 **HcpR heme binding pocket**

240 We previously determined the structure of the ΔCHcpR sensing domain and tried to
241 identified heme binding sites. Although our research found two hydrophobic pockets, they were not
242 large enough to accommodate a heme molecule (7). Using resonance Raman spectroscopy, we
243 also determined that heme-bound HcpR is primarily in a 6-coordinate state, with one of the axial
244 bonds being weaker and easily broken. Thus, it is likely that the two side chains involved in
245 coordination are essential for activating HcpR. To search for potential heme-binding sites, we use
246 AutoDock Vina using the structure of the dimer as the target (22). The highest-scoring prediction
247 positioned the heme group at a crevice located at the interface of the two subunits (Fig. 5A).
248 Particularly the DBD of chain A and the flap of the SD of chain B. Crucially, two residues, Met68 and
249 His149, appear primed in the pocket to coordinate the heme iron (Fig. 5B). Apart from the heme iron
250 coordination, many residues from both chains in and around the pocket are in possible positions to
251 form contacts with heme. These include hydrophobic interactions from Val69, Ile78, Pro71, Pro100,
252 Met145, and Ile148, and hydrogen bonding and ionic/salt bridge interactions between the acid
253 groups of heme and Lys146, Ser225, and Arg226 (Fig. 5C). In the crystal structure this pocket is
254 occupied by a portion of the polyhistidine-tail and the TEV protease site that transverses across the
255 tunnel created by the flap of molecule B and the DBD of molecule A (Figure X). The hydrophobic
256 character of the pocket induces the tail interaction.

257 To determine the importance of Met68 or His149 for HcpR activation, we mutated these
258 residues to alanine and plasmid complemented an HcpR deficient strain of *P. gingivalis* (V2807) [8].
259 Crucially, *P. gingivalis* lacking HcpR does not grow in physiologically relevant concentrations of NO_2^-
260 , thus a strain with an inactive or deficient HcpR cannot tolerate elevated NO_2^- levels. With
261 treatment with NO_2^- we saw a significant decrease in the growth of the M68A strain at 1mM NO_2^-
262 and no growth at the higher concentration of 2mM (Fig 4A). The double mutant of M68A/H149A
263 could not grow at either concentration of NO_2^- and was comparable to the ΔCHcpR negative control
264 that completely lacks the DNA binding domain. Unexpectedly, with the H149A mutant we saw no
265 significant decrease in growth at either concentration of NO_2^-.

266 To measure activity of the HcpR mutants, we assessed transcription of the *hcp* gene *in vivo*.
267 In agreement with the growth studies, we saw a significant decrease of *hcp* transcript in the M68A
268 complemented strain (Fig. 4B). However, there was still modest expression of *hcp*, which explains
269 why the M68A strain exhibited some growth when compared to the L156* negative control at the
270 lower concentration of nitrite. With the M68A/H149A double mutant we saw *hcp* transcript levels
271 comparable to that of the negative control. With the H149A mutant we saw no significant decrease
272 in *hcp* transcript levels.

273 To confirm expression and growth data we expressed and purified the M68A and
274 M68A/H149A mutant HcpRs and compared them to wildtype HcpR spectroscopically. Both strains
275 were purified at similar concentrations and purities to the wild type protein using cobalt affinity
276 resin. The M68A/H149A double mutant did not bind heme effectively, which can be easily seen in
277 the loss of color of the protein after reconstitution with heme and desalting (Fig. 5A). The UV-Vis
278 spectrum revealed very little of the heme remained bound to the protein as evidence by lack of a

Soret band (Fig 5B). The M68A mutant was still capable of binding heme and retains its coloring. However, there were subtle changes in the UV-Vis spectrum under anaerobic reduced conditions: there was a shift in the main Soret peak from 428nm in the wildtype HcpR to 426nm in M68A HcpR (Fig. 5C). There is also significant flattening of the α-β peaks at 533nm and 550nm. As the Soret spectrum arises from the heme-protein interactions, this indicates that there are changes in the heme binding pocket of M68A HcpR.

Interdomain interactions are critical for generating a heme binding pocket

As we have shown, the formation of the heme binding site depends on the chain A DBD being in a conformation that allows it to form contacts with the flap region of Chain B. Arg226 of chain A is of particular interest, as it forms polydentate interactions with two backbone residues in the flap loop of chain B. The effect of this interaction is evident when comparing the FL-HcpR with the ΔCHcpR. The two structures superimpose with an RMSD of 0.564 Å (Fig. 6A). There is an ~13.7 Å difference in the location of the flap region along residues 69-75 (Fig. 6B). These contacts are reflected in the B-factors of these regions in the two structures: the flap region of chain B in the FL-HcpR has lower B-factors than their corresponding regions in chain A (Fig. S5). The interdomain interactions create a divergence in the putative heme binding pocket size between the HcpR molecules in the dimer (Fig 6C). The pocket of FL-HcpR chain A aligns near perfectly with both chains of ΔCHcpR and is significantly smaller because there are no interactions between domains (Fig 6A). In both chains of ΔCHcpR and chain A of FL-HcpR, the pocket size is approximately 520 $Å^3$. In chain B of FL-HcpR, the pocket size increases to approximately 1100 $Å^3$. This increased pocket size is much easier to accommodate heme, which has a volume of ~510 $Å^3$. This interaction demonstrates that the orientation of the DNA-binding domain can influence folding of the sensing domain.

The difference in conformation between the two DBDs' reflects the hinge region's flexibility along residues 152-156 around which the DBDs move. In the crystal structure of FL-HcpR, the orientation of the DNA binding domain is also influenced by crystal packing forces (Fig. S6). These forces can stabilize the E helix in an extended form or allow the SD to form contacts with the DBD. When the DBD is allowed to contact the SD, as seen in the case of chain A DBD and chain B SD, the pocket is stabilized. In the crystal structure, the pocket that forms is further occupied by a portion of the N-terminus of an adjacent homo-dimer in the crystal lattice. Crucially, the pocket appears smaller in the SD of chain A and the ΔCHcpR structure due to the absence of the DBD interactions.

Discussion

In this study, we present the structure of the full-length HcpR. The protein crystallizes in a peculiar form, with significant asymmetry in the C-terminal DNA binding domain that is not uncommon in CRP family regulators [3]. The off-state may be represented by the extended E helix in chain B. This structure is present in both chains of the NO sensor DNR [26]. However, it is unlikely that HcpR will adopt this structure in the off-state. The residues forming the leucine zipper motif that stabilize the homodimer do not extend past the hinge region at Leu153. After this point, most residues forming the motif have polar, hydrophilic side chains. Previously, we have demonstrated, using SAXS ensemble optimization modeling, that the DNA binding domain of Apo-HcpR can adopt

320 several different conformations in solution [27]. Thus, it is possible that the off form is an ensemble of
321 different combinations, and activation of HcpR stabilizes the DNA binding domain into an
322 orientation with accessible recognition helices.

323 The two conformations of the DBD can also be seen in some crystal structures of CooA and
324 CAP. In HcpR, as in CooA, the DNA binding domain of chain B is in the fully "off" conformation with
325 the recognition helix facing in towards the protein [3]. The recognition helix of chain A is partially
326 accessible; however, it is not in the fully outward facing orientation as seen in the structure of CAP
327 bound to DNA. The heterogeneity of the two chains reflects the flexibility of the hinge region around
328 which the DNA binding domains move and is important for creating the putative heme binding
329 pocket. Moreover, the presence of the two conformations suggests that they are in a dynamic
330 equilibrium in solution.

331 Guided by docking and mutagenesis studies, we interrogated the enlarged pocket in chain B
332 as a putative heme-binding location. We identified two important residues in heme binding and
333 activation, Met68 and His149. Both side chains are extended into the pocket and are in prime
334 position to coordinate heme. Loss of Met68 severely inhibits the activity of HcpR. The single amino
335 acid mutation decreases the activity by <10%. However, there is still a modicum of activity as
336 measured using qRT-PCR. This may explain how the M68A complemented strain can persist at the
337 lower nitrite concentration. Nitrite is bacteriostatic at these levels. It is possible a small amount of
338 HcpR activity overtime can produce enough *hcp* transcript to allow for diminished growth. Loss of
339 His149 does not affect the activity of HcpR. However, the M68/H149 double mutant HcpR has no
340 activity, like ΔCHcpR. The purified M68A/H149A HcpR does not bind heme, explaining the activity
341 observed *in vivo*. The His149 may play a role in heme coordination and stability of co-factor binding
342 but appears to not play an indispensable role in the allosteric network that governs HcpR
343 activation.

344 In the CRP family, distinct regulators have evolved to sense a wide variety of biologically
345 relevant molecules involved in respiration, stress response, and metabolism. These regulators are
346 based on a common modular design: (1) ligand binding β-barrels attached to a (2) central α-helix
347 leucine zipper pair connected to a (3) C-terminal HTH DNA binding domain by a (4) flexible hinge
348 region [24,28–32]. Ligand binding appears to work on each of the modular parts, influencing their
349 interactions and stabilizing the DNA binding domain in an "On" conformation (one in which the
350 recognition helices are oriented such that the major groove of DNA is accessible). Despite their
351 similar structural orientation and folds, activation depends on the exact nature of the ligand-
352 induced reorganization of the β-barrel sensing domain and its effect on the allosteric networks
353 communicating between the ligand binding domain and the DNA binding domain. Thus, among the
354 CRP family members, key residues have little conservation (such as those involved in ligand
355 interaction or co-factor binding).

356 This is reflected in the crystal structures and mechanisms of other well studied CRP
357 members. In CAP, cyclic-AMP forms contacts with residues near the hinge region, extending the
358 dimerization helix by 3 turns and forming a coiled-coil motif that stabilizes the orientation of the
359 DNA binding domain [33]. In CooA, binding of CO to heme displaces an N-terminal proline residue
360 that frees up this region to form bridging contacts between the sensing domain and the DNA
361 binding domain [34]. In the halogen sensor CprK, ligand binding leads to a re-orientation of the

362 binding pocket, decreasing its volume, that ultimately affects the position of key residues on the
363 "flap" region that stabilize the DNA binding domain through formation of new contacts [28].

364 Despite CooA being the most well characterized heme binding CRP protein, several
365 differences between CooA and HcpR are evident in the crystal structures. Although HcpR does
366 have a proline residue near the N-terminus, the two helices adjacent to the N-terminus are well
367 ordered and are not in a position that is located near the putative heme binding site. As previously
368 mentioned, the extended loop region of HcpR corresponds to the heme binding location in CooA. In
369 CooA, this region is shortened to accommodate the heme and is evident in the sequence of
370 overlays of HcpR and CooA (FigS2). Thus, the heme binding location of HcpR is different from CooA
371 and is likely "below" it (closer towards the C-terminal domain). The CooA mechanism of activation
372 (the "Velcro" model) involves CO dependent displacement of the N-terminal proline residue bound
373 to heme allowing the N-terminus to form contacts with the DNA binding domain [34]. Based on the
374 structure and heme binding studies here, it is likely that mechanism of HcpR is distinct from CooA.

375 DNR is a CRP family protein found in *Pseudomonas* that utilizes heme to sense NO, much
376 like HcpR [35,36]. DNR shares the highest sequence identity of the characterized CRP members with
377 HcpR at 20%. The mechanism of DNR activation, although not well understood, differs from that of
378 CooA. A significant conformational change in the crystal structure of DNR would be required for it
379 to bind DNA, but the changes differ from those of CooA. Note that the position of the sensing
380 domain in DNR structure is rotated by 60 degrees compared to the inactive form of CooA [26].
381 Mutagenesis and heme binding studies reveal significant ligand switching occurs to accommodate
382 mutations to heme coordinating residues [37]. As there is little overlap in the conservation of key
383 residues between DNR and HcpR it is difficult to speculate how their mechanisms may be
384 analogous.

385 One possible mechanism for HcpR mirrors the pocket rearrangement CprK undergoes upon
386 ligand binding. NO binding to heme displaces Met68. This displacement rearranges the pocket,
387 shifting the flap region out along residues 72-75 into a position to make contacts with the DNA
388 binding domain. These contacts stabilize the DNA binding domain into a position with the
389 recognition helices accessible to DNA. This putative mechanism is attractive for several reasons.
390 The location of the flap is very close to Met68 and displacement of the side chain can easily
391 influence the flap location. This is bolstered by the highly conserved flap sequence in 72-75, with
392 side chains that are accessible (Fig. 3). Among the CRP structures solved in the active formation,
393 all adopt a similar DNA binding domain conformation in the active form. This would allow for the
394 Ser72, Lys74, and Gln75 to form hydrogen bonds or salt bridges with the DNA binding domain.
395 Furthermore, we have shown that this region capable of shifting when comparing the ΔCHcpR and
396 FL-HcpR structures. This region is extended out by ~14Å in the FL-HcpR structure, indicating the
397 flexibility of this region to allow wide movements (Fig. 8B).

398 This can be illustrated using AlphaFold 3 to model the DNA binding domains in the active
399 DNA bound form onto the crystal structure of FL-HcpR with heme docked (Fig. S6A) [21]. The
400 conserved flap residues form an interface with conserved residues adjacent to the recognition helix
401 (Fig. S6B). This includes potential hydrogen bonding between Asn192 and Ser72 and the backbone
402 at Gly73 and a potential network of ionic or hydrogen bonding interactions between Lys 74 and
403 Gln75 and Lys183, Glu184, and Asp187. Additionally, Phe189 appears positioned at the entrance to

404 the heme pocket, lending potential for hydrophobic interactions to occur here. As can be seen in a
405 sequence overlay, the residues on the flap and the "turn" of the helix-turn-helix motif are highly
406 conserved between different species of *Porphyromonas* and *Prevotella,* indicating their potential
407 importance in stabilizing the active form.

408 Further experimental support is needed to confirm this hypothesis. Despite our attempts,
409 we were unable to obtain viable crystals of the heme-protein complex for this report. Further
410 studies involving the dynamics of NO binding and its effects on the nature of the heme pocket and
411 DNA binding will help clarify the molecular mechanism of HcpR and the allosteric interactions that
412 govern its activation.

413

414 **Figure Legends**

415 **Figure 1 - Overview of the crystal structure of full length HcpR**. (A) Ribbon diagram of the HcpR
416 shown in forward and 90º side view showing orientation of the N-terminal sensing domain and C-
417 terminal DNA binding domain. Chain A is colored in blue and Chain B is colored in green. The two
418 chains form a homodimer. (B) Dimerization helices of HcpR. The homodimer is stabilized by
419 hydrophobic interactions between symmetry related Met, Leu, and Ile residues. (C) Highlight of the
420 asymmetry of the DNA binding domains of chains A and B. Helix E of chain A is broken at the hinge
421 region at residue 152 where Helix E of chain B is extended through residue 170. (D) Superimposing
422 chains A and B highlights the asymmetry of the DNA binding domains. The DBD of chain A is rotated
423 166º with respect to chain B. (E) Inset of boxed region in panel (A). The flap region of chain B is
424 angled backwards 39.6 º create a pocket in the SD of chain B.

425 **Figure 2 - Comparison of the overall fold and conformational differences between HcpR and**
426 **CooA.** (A) Stereo view of HcpR (green) and CooA (purple) dimers depicting the overall organization
427 of each protein. The N-terminal domain of HcpR (extending from residue 1-127) is slightly larger
428 than that of CooA (extending from residues 2-107). (B) Superposition of the HcpR-CooA overlay at
429 the location of CooA binding site. The extended loop region of HcpR (89-93) occupies this region.

430 **Figure 3 - Heme docks into the hydrophobic pocket of HcpR.** (A) Overview of heme docking in the
431 HcpR pocket. Heme docks at the interface between chain B SD and middle portion of helix E of
432 chain A. (B) Side chains present in the putative heme pocket. Both Met68 and His149, residues
433 commonly implicated in heme coordination, are optimally located in the pocket to coordinate the
434 heme iron. (C) Side chains present in the heme pocket that form potential contacts with docked
435 heme.

436 **Figure 4 - Met68 is important for proper function of HcpR.** (A) Growth of ΔHcpR *P. gingivalis*
437 complemented with WT and mutant HcpRs (L156* mutant lacks the DNA binding domain and
438 serves as a negative control). Complemented strains were grown in 1mM NO_2 or 2mM NO_2 for 24
439 hours in Tryptic Soy Broth. After incubation the optical density at 600nm was used to assess
440 growth. (B) Complemented ΔHcpR *P. gingivalis* strains growing in mid-log phase were exposed to
441 0.2mM NO_2 for 15 minutes and collected. The level of *hcp* transcript was assessed via qRT-PCR to
442 assess activity of HcpR mutants. Expression levels of *hcp* mRNA are normalized to the 16s subunit
443 mRNA.

Figure 5 - Met68 and His149 are necessary for proper binding of heme to HcpR. (A) Heme binding of WT, M68A, and M68A/H149A HcpR – the amber color of WT and M68A purified protein indicates the presence of heme in the sample. (B) Spectra of the reduced, heme bound WT-HcpR and the M68A/H149A double mutant HcpR. The loss of the Soret peak in the M68A/H149A HcpR indicates loss of heme binding. (C) Spectra of the reconstituted WT HcpR and M68A HcpR under reduced, anaerobic conditions. Changes in the location and form of the Soret peak indicates changes in the heme binding nature of the M68A HcpR.

Figure 6 - Structural alignment of full length HcpR and ΔCHcpR highlights the interdomain interactions that stabilize the heme pocket. (A) Structural overlay of the full length HcpR (green) and the C-terminal truncated ΔCHcpR (red). The structures overlay with an RMSD of 0.564Å. (B) Zoomed in view of boxed region in (A) of the flap region in chain B of HcpR compared to that of chain B in ΔCHcpR. The flap region of HcpR has shifted out by 13.7Å, enlarging the hydrophobic pocket. (C) Surface view of the boxed region in (A) of the pocket present in the full length HcpR and the subsequent position and ΔCHcpR.

Figure S1 - Sequence alignments of HcpR found in *Porphyromonas* and *Prevotella* species. Conservations of residues is graded on a scale of 1 to 11, where 1 indicates no conservation at that site and 10 (+) near identical conservation and 11 (*) indicates a residue is completely conserved across all sequences.

Figure S2 - Arg226 and the flap region hydrogen bond. Arg226 forms to hydrogen bonds with the flap region along the backbone of Val69 and Gly70.

Figure S3 - Sequence alignment of CooA and HcpR. The sequence alignment highlights the extended loop region of HcpR that occupies the heme binding site in CooA. Green highlight represents β-sheet structures and teal highlights represents α-helices.

Figure S4 - Comparison of overall fold and conformational differences between HcpR and CAP. (A) Stereo view of HcpR (green) and CAP (cyan) dimers depicting the overall organization of each protein. The N-terminal domain of HcpR (extending from residue 1-127) is larger than that of CAP (extending from residues 1-110). (B) Superposition of the HcpR-CAP overlay at the location of cyclic-AMP binding site. The extended loop region of HcpR (89-93) partially occludes this region.

Figure S5 - B-factors in structure of HcpR. Structural representations of B-factors on a scale of 18 (green)-148 (yellow).

Figure S6 - Crystal packing in the full-length structure of HcpR. The individual homo-dimer represented in blue and green chains with crystal contacts with adjacent homodimers in the crystal lattice.

Figure S7 - Model of the full length HcpR structure in the active confirmation. (A) Overview of the HcpR homo-dimer in the active confirmation bound to DNA. (B) Conserved residues that form the interface between the flap along residues 72-75 and the DBD along residues 183-192 with the sequence alignments of each region.

482 **Data Availability.** The crystal structure data have been deposited to Protein Data Bank (PDB)
483 with a title "Crystal Structure of the Transcriptional Regulator HcpR from *Porphyromonas*
484 *gingivalis*" and assigned the following accession code(s): PDB ID 9DAY

485

486 **Funding information:**
487 This work was supported by NIH/NIDCR grant RO1DE023304 "Nitrosative Stress
488 and Oral Bacteria (J. P. Lewis)".

489

490 Table 1: Data Collection and refinement statistics

Data Collection Statistics	
Space group	$P\ 2_1\ 2_1\ 2_1$
Unit-cell *a, b, c* (Å)	106.260, 106.303, 116.773
Resolution (Å) Total reflections	29.13–2.30 (2.36 – 2.30) 711884 (55391)
Unique reflections	59441 (4590)
Redundancy	12.0 (12.1)
Completeness (%)	99.9 (100.0)
Average **I**/σ(I)	33.7 (4.6)
R_{merge} (%)[a]	5.9 (60.1)
Refinement Statistics	
Resolution (Å)	29.13-2.30 (2.38-2.30)
No. of reflections	59146 (2542)
R_{work} (%)	21.57 (26.87)
R_{free} (%)[b]	26.47 (32.05)
R.m.s.d. bonds (Å)	0.002
R.m.s.d. angles (°)	0.5800
Dihedral angles	

Most favored (%)	94.4
Allowed (%)	4.6
Average B (Å^2) / atoms	
All atoms	69.00
Protein Ligand Solvent **Number of non-hydrogen atoms**	71.01 56.86 51.31 7632
Macromolecules Ligands Water	7221 48 363
Protein residues	926

[a]$R_{merge} = \Sigma_{hkl}\Sigma_i|I_i(hkl) - \langle I(hkl)\rangle|/\Sigma_{hkl}\Sigma_i I_i(hkl)$. [b]$R_{free}$ was calculated from 5% randomly selected reflection for cross-validation. All other measured reflections were used during refinement.

508 References

509

510 (1) Rodionov, D. A.; Dubchak, I. L.; Arkin, A. P.; Alm, E. J.; Gelfand, M. S. Dissimilatory Metabolism of
511 Nitrogen Oxides in Bacteria: Comparative Reconstruction of Transcriptional Networks. *PLoS*
512 *Comput Biol* **2005**, *1* (5), e55.

513 (2) Cole, J. A. Anaerobic Bacterial Response to Nitric Oxide Stress: Widespread Misconceptions and
514 Physiologically Relevant Responses. *Molecular Microbiology*. John Wiley and Sons Inc July 1,
515 2021, pp 29–40. https://doi.org/10.1111/mmi.14713.

516 (3) Lanzilotta, W. N.; Schuller, D. J.; Thorsteinsson, M. V; Kerby, R. L.; Roberts, G. P.; Poulos, T. L.
517 Structure of the CO Sensing Transcription Activator CooA. *Nat Struct Biol* **2000**, *7* (10), 876–880.
518 https://doi.org/10.1038/82820 [doi].

519 (4) Lawson, C. L.; Swigon, D.; Murakami, K. S.; Darst, S. A.; Berman, H. M.; Ebright, R. H. Catabolite
520 Activator Protein: DNA Binding and Transcription Activation. *Current Opinion in Structural Biology*.
521 Elsevier Ltd 2004, pp 10–20. https://doi.org/10.1016/j.sbi.2004.01.012.

522 (5) Körner, H.; Sofia, H. J.; Zumft, W. G. Phylogeny of the Bacterial Superfamily of Crp-Fnr
523 Transcription Regulators: Exploiting the Metabolic Spectrum by Controlling Alternative Gene
524 Programs. *FEMS Microbiology Reviews*. Lehrstuhl fur Mikrobiologie, Universitat Karlsruhe, PF
525 6980, D-76128 Karlsruhe, Germany. December 2003, pp 559–592.
526 https://doi.org/10.1016/S0168-6445(03)00066-4.

527 (6) Zhou, A.; Chen, Y. I.; Zane, G. M.; He, Z.; Hemme, C. L.; Joachimiak, M. P.; Baumohl, J. K.; He, Q.;
528 Fields, M. W.; Arkin, A. P.; Wall, J. D.; Hazen, T. C.; Zhou, J. Functional Characterization of Crp/Fnr-
529 Type Global Transcriptional Regulators in Desulfovibrio Vulgaris Hildenborough. *Appl Environ*
530 *Microbiol* **2012**, *78* (4), 1168–1177. https://doi.org/10.1128/AEM.05666-11.

531 (7) Cadby, I. T.; Faulkner, M.; Cheneby, J.; Long, J.; Van Helden, J.; Dolla, A.; Cole, J. A. Coordinated
532 Response of the Desulfovibrio Desulfuricans 27774 Transcriptome to Nitrate, Nitrite and Nitric
533 Oxide. *Sci Rep* **2017**, *7* (1). https://doi.org/10.1038/s41598-017-16403-4.

534 (8) Lewis, J. P.; Yanamandra, S. S.; Anaya-Bergman, C. HcpR of Porphyromonas Gingivalis Is Required
535 for Growth under Nitrosative Stress and Survival within Host Cells. *Infect Immun* **2012**, *80* (9),
536 3319–3331. https://doi.org/10.1128/IAI.00561-12.

537 (9) Hezel, M. P.; Weitzberg, E. The Oral Microbiome and Nitric Oxide Homoeostasis. *Oral Dis* **2015**, *21*
538 (1), 7–16. https://doi.org/10.1111/odi.12157 [doi].

539 (10) Gyurko, R.; Boustany, G.; Huang, P. L.; Kantarci, A.; Van Dyke, T. E.; Genco, C. A.; Gibson 3rd, F. C.
540 Mice Lacking Inducible Nitric Oxide Synthase Demonstrate Impaired Killing of Porphyromonas
541 Gingivalis. *Infect Immun* **2003**, *71* (9), 4917–4924.

542 (11) Miller, D. P.; Hutcherson, J. A.; Wang, Y.; Nowakowska, Z. M.; Potempa, J.; Yoder-Himes, D. R.;
543 Scott, D. A.; Whiteley, M.; Lamont, R. J. Genes Contributing to Porphyromonas Gingivalis Fitness
544 in Abscess and Epithelial Cell Colonization Environments. *Front Cell Infect Microbiol* **2017**, *7*, 378.
545 https://doi.org/10.3389/fcimb.2017.00378.

(12) Boutrin, M. C.; Wang, C.; Aruni, W.; Li, X.; Fletcher, H. M. Nitric Oxide Stress Resistance in Porphyromonas Gingivalis Is Mediated by a Putative Hydroxylamine Reductase. *J Bacteriol* **2012**, *194* (6), 1582–1592. https://doi.org/10.1128/JB.06457-11.

(13) Belvin, B. R.; Gui, Q.; Hutcherson, J. A.; Lewis, J. P. The Porphyromonas Gingivalis Hybrid Cluster Protein Hcp Is Required for Growth with Nitrite and Survival with Host Cells. *Infect Immun* **2019**, *87* (4). https://doi.org/10.1128/IAI.00572-18.

(14) Liebl, U.; Lambry, J. C.; Vos, M. H. Primary Processes in Heme-Based Sensor Proteins. *Biochim Biophys Acta Proteins Proteom* **2013**, *1834* (9), 1684–1692. https://doi.org/10.1016/j.bbapap.2013.02.025.

(15) Shimizu, T.; Huang, D.; Yan, F.; Stranava, M.; Bartosova, M.; Fojtíková, V.; Martínková, M. Gaseous O2, NO, and CO in Signal Transduction: Structure and Function Relationships of Heme-Based Gas Sensors and Heme-Redox Sensors. *Chemical Reviews*. American Chemical Society July 8, 2015, pp 6491–6533. https://doi.org/10.1021/acs.chemrev.5b00018.

(16) Coyle, C. M.; Puranik, M.; Youn, H.; Brøndsted Nielsen, S.; Williams, R. D.; Kerby, R. L.; Roberts, G. P.; Spiro, T. G. Activation Mechanism of the CO Sensor CooA: Mutational and Resonance Raman Spectroscopic Studies. *Journal of Biological Chemistry* **2003**, *278* (37), 35384–35393. https://doi.org/10.1074/jbc.M301000200.

(17) Roberts, M. G.; Dent, M. R.; Ramos, S.; Thielges, M. C.; Burstyn, J. N. Probing Conformational Dynamics of DNA Binding by CO-Sensing Transcription Factor, CooA. *J Inorg Biochem* **2024**, *259*. https://doi.org/10.1016/j.jinorgbio.2024.112656.

(18) Jones, K. R.; Belvin, B. R.; Macrina, F. L.; Lewis, J. P. Sequence and Characterization of Shuttle Vectors for Molecular Cloning in Porphyromonas, Bacteroides and Related Bacteria. *Mol Oral Microbiol* **2020**, *35* (4), 181–191. https://doi.org/10.1111/omi.12304.

(19) Meng, E. C.; Goddard, T. D.; Pettersen, E. F.; Couch, G. S.; Pearson, Z. J.; Morris, J. H.; Ferrin, T. E. UCSF ChimeraX: Tools for Structure Building and Analysis. *Protein Science* **2023**, *32* (11). https://doi.org/10.1002/pro.4792.

(20) Pettersen, E. F.; Goddard, T. D.; Huang, C. C.; Meng, E. C.; Couch, G. S.; Croll, T. I.; Morris, J. H.; Ferrin, T. E. UCSF ChimeraX: Structure Visualization for Researchers, Educators, and Developers. *Protein Science* **2021**, *30* (1), 70–82. https://doi.org/10.1002/pro.3943.

(21) Abramson, J.; Adler, J.; Dunger, J.; Evans, R.; Green, T.; Pritzel, A.; Ronneberger, O.; Willmore, L.; Ballard, A. J.; Bambrick, J.; Bodenstein, S. W.; Evans, D. A.; Hung, C. C.; O'Neill, M.; Reiman, D.; Tunyasuvunakool, K.; Wu, Z.; Žemgulytė, A.; Arvaniti, E.; Beattie, C.; Bertolli, O.; Bridgland, A.; Cherepanov, A.; Congreve, M.; Cowen-Rivers, A. I.; Cowie, A.; Figurnov, M.; Fuchs, F. B.; Gladman, H.; Jain, R.; Khan, Y. A.; Low, C. M. R.; Perlin, K.; Potapenko, A.; Savy, P.; Singh, S.; Stecula, A.; Thillaisundaram, A.; Tong, C.; Yakneen, S.; Zhong, E. D.; Zielinski, M.; Žídek, A.; Bapst, V.; Kohli, P.; Jaderberg, M.; Hassabis, D.; Jumper, J. M. Accurate Structure Prediction of Biomolecular Interactions with AlphaFold 3. *Nature* **2024**, *630* (8016), 493–500. https://doi.org/10.1038/s41586-024-07487-w.

584 (22) Sievers, F.; Wilm, A.; Dineen, D.; Gibson, T. J.; Karplus, K.; Li, W.; Lopez, R.; McWilliam, H.;
585 Remmert, M.; Soding, J.; Thompson, J. D.; Higgins, D. G. Fast, Scalable Generation of High-Quality
586 Protein Multiple Sequence Alignments Using Clustal Omega. *Mol Syst Biol* **2011**, *7*, 539.
587 https://doi.org/10.1038/msb.2011.75 [doi].

588 (23) Waterhouse, A. M.; Procter, J. B.; Martin, D. M. A.; Clamp, M.; Barton, G. J. Jalview Version 2-A
589 Multiple Sequence Alignment Editor and Analysis Workbench. *Bioinformatics* **2009**, *25* (9), 1189–
590 1191. https://doi.org/10.1093/bioinformatics/btp033.

591 (24) Schultz, S. C.; Shields, G. C.; Steitz, T. A. Crystal Structure of a CAP-DNA Complex: The DNA Is Bent
592 by 90 Degrees. *Science* **1991**, *253* (5023), 1001–1007.

593 (25) Trott, O.; Olson, A. J. AutoDock Vina: Improving the Speed and Accuracy of Docking with a New
594 Scoring Function, Efficient Optimization, and Multithreading. *J Comput Chem* **2010**, *31* (2), 455–
595 461. https://doi.org/10.1002/jcc.21334.

596 (26) Giardina, G.; Rinaldo, S.; Castiglione, N.; Caruso, M.; Cutruzzola, F. A Dramatic Conformational
597 Rearrangement Is Necessary for the Activation of DNR from Pseudomonas Aeruginosa. Crystal
598 Structure of Wild-Type DNR. *Proteins* **2009**, *77* (1), 174–180. https://doi.org/10.1002/prot.22428;
599 10.1002/prot.22428.

600 (27) Belvin, B. R.; Musayev, F. N.; Burgner, J.; Scarsdale, J. N.; Escalante, C. R.; Lewis, J. P.; IUCr.
601 Nitrosative Stress Sensing in *Porphyromonas Gingivalis* : Structure of and Heme Binding by the
602 Transcriptional Regulator HcpR. *Acta Crystallogr D Struct Biol* **2019**, *75* (4), 437–450.
603 https://doi.org/10.1107/S205979831900264X.

604 (28) Levy, C.; Pike, K.; Heyes, D. J.; Joyce, M. G.; Gabor, K.; Smidt, H.; van der Oost, J.; Leys, D.
605 Molecular Basis of Halorespiration Control by CprK, a CRP-FNR Type Transcriptional Regulator.
606 *Mol Microbiol* **2008**, *70* (1), 151–167. https://doi.org/10.1111/j.1365-2958.2008.06399.x [doi].

607 (29) Passner, J. M.; Schultz, S. C.; Steitz, T. A. Modeling the CAMP-Induced Allosteric Transition Using
608 the Crystal Structure of CAP-CAMP at 2.1 A Resolution. *J Mol Biol* **2000**, *304* (5), 847–859.
609 https://doi.org/10.1006/jmbi.2000.4231 [doi].

610 (30) Roberts, G. P.; Kerby, R. L.; Youn, H.; Conrad, M. CooA, a Paradigm for Gas Sensing Regulatory
611 Proteins. *J Inorg Biochem* **2005**, *99* (1), 280–292. https://doi.org/S0162-0134(04)00339-3 [pii].

612 (31) Kuchinskas, M.; Li, H.; Conrad, M.; Roberts, G.; Poulos, T. L. The Role of the DNA-Binding Domains
613 in CooA Activation. *Biochemistry* **2006**, *45* (23), 7148–7153. https://doi.org/10.1021/bi052609o
614 [doi].

615 (32) Fic, E.; Bonarek, P.; Gorecki, A.; Kedracka-Krok, S.; Mikolajczak, J.; Polit, A.; Tworzydlo, M.;
616 Dziedzicka-Wasylewska, M.; Wasylewski, Z. CAMP Receptor Protein from Escherichia Coli as a
617 Model of Signal Transduction in Proteins - A Review. *Journal of Molecular Microbiology and*
618 *Biotechnology*. May 2009, pp 1–11. https://doi.org/10.1159/000178014.

619 (33) Popovych, N.; Tzeng, S. R.; Tonelli, M.; Ebright, R. H.; Kalodimos, C. G. Structural Basis for CAMP-
620 Mediated Allosteric Control of the Catabolite Activator Protein. *Proc Natl Acad Sci U S A* **2009**, *106*
621 (17), 6927–6932. https://doi.org/10.1073/pnas.0900595106 [doi].

(34) Tripathi, S.; Poulos, T. L. Testing the N-Terminal Velcro Model of CooA Carbon Monoxide Activation. *Biochemistry* **2018**, *57* (21), 3059–3064. https://doi.org/10.1021/acs.biochem.8b00359.

(35) Giardina, G.; Rinaldo, S.; Johnson, K. A.; Di Matteo, A.; Brunori, M.; Cutruzzola, F. NO Sensing in Pseudomonas Aeruginosa: Structure of the Transcriptional Regulator DNR. *J Mol Biol* **2008**, *378* (5), 1002–1015. https://doi.org/10.1016/j.jmb.2008.03.013 [doi].

(36) Castiglione, N.; Rinaldo, S.; Giardina, G.; Cutruzzola, F. The Transcription Factor DNR from Pseudomonas Aeruginosa Specifically Requires Nitric Oxide and Haem for the Activation of a Target Promoter in Escherichia Coli. *Microbiology (Reading)* **2009**, *155* (Pt 9), 2838–2844. https://doi.org/10.1099/mic.0.028027-0; 10.1099/mic.0.028027-0.

(37) Cutruzzola, F.; Arcovito, A.; Giardina, G.; della Longa, S.; D'Angelo, P.; Rinaldo, S. Distal-Proximal Crosstalk in the Heme Binding Pocket of the NO Sensor DNR. *Biometals* **2014**, *27* (4), 763–773. https://doi.org/10.1007/s10534-014-9770-3 [doi].

Figure 1

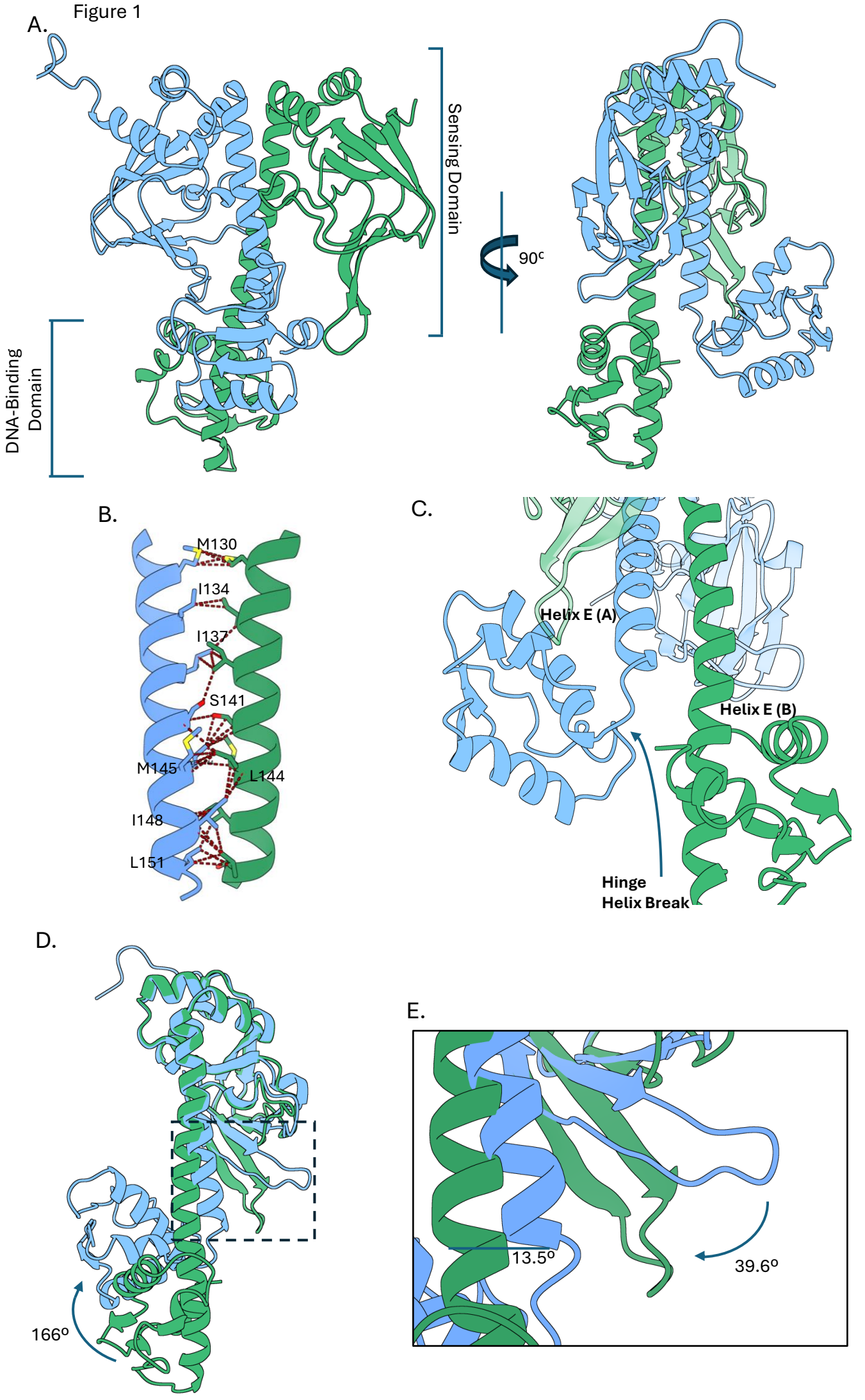
A.
Sensing Domain
DNA-Binding Domain
90°
B.
M130
I134
I137
S141
M145
L144
I148
L151
C.
Helix E (A)
Helix E (B)
Hinge
Helix Break
D.
166°
E.
13.5°
39.6°

Figure 2

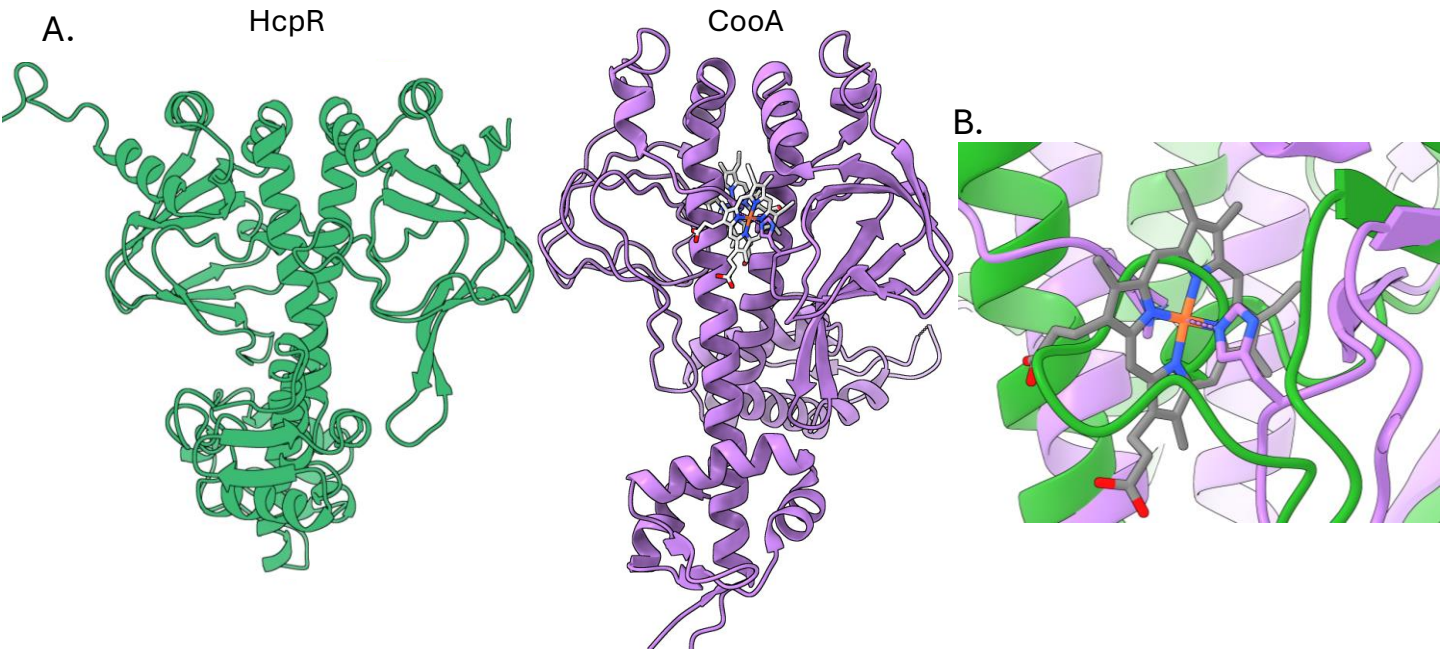

Figure 3

A.

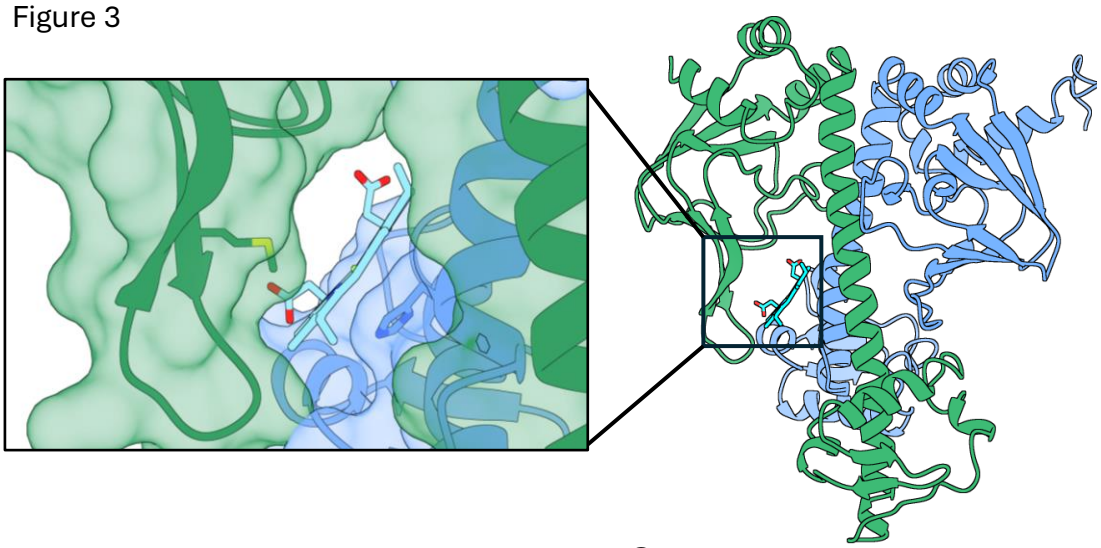

B.

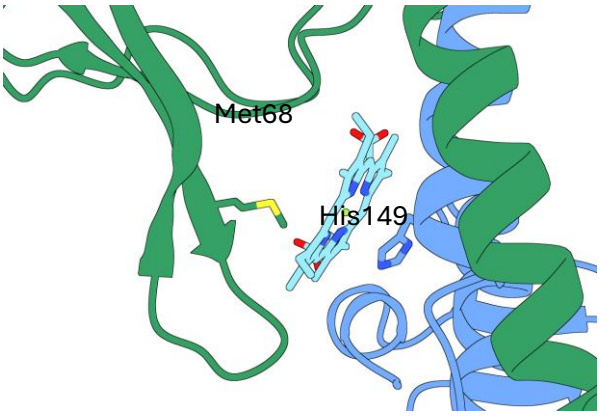
Met68
His149

C.

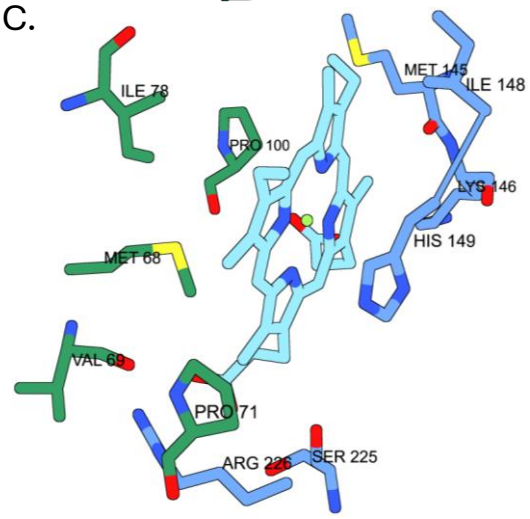
ILE 78
PRO 100
MET 145
ILE 148
LYS 146
HIS 149
MET 68
VAL 69
PRO 71
ARG 226
SER 225

Figure 4

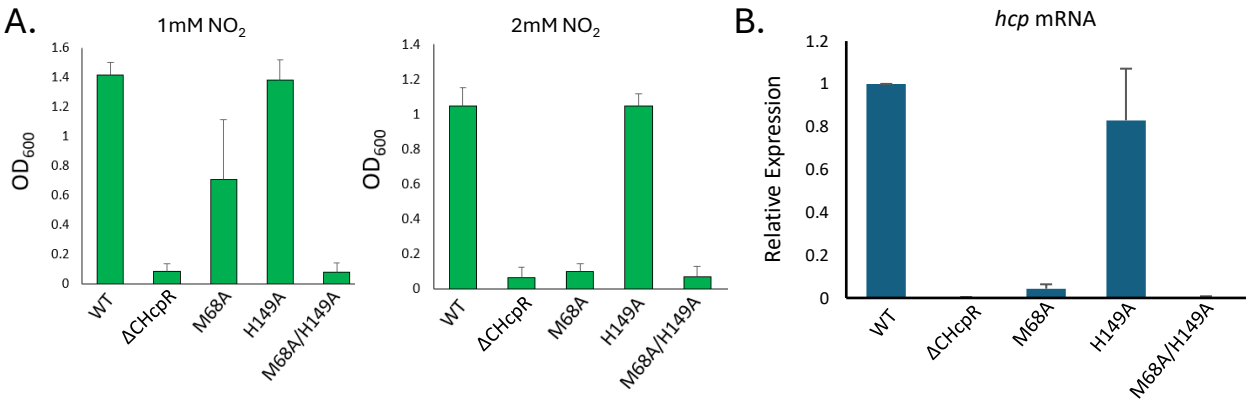
A.
1mM NO_2
OD_{600}
1.6
1.4
1.2
1
0.8
0.6
0.4
0.2
0
WT
ΔCHcpR
M68A
H149A
M68A/H149A
2mM NO_2
OD_{600}
1.4
1.2
1
0.8
0.6
0.4
0.2
0
WT
ΔCHcpR
M68A
H149A
M68A/H149A
B.
hcp mRNA
Relative Expression
1.2
1
0.8
0.6
0.4
0.2
0
WT
ΔCHcpR
M68A
H149A
M68A/H149A

Figure 5

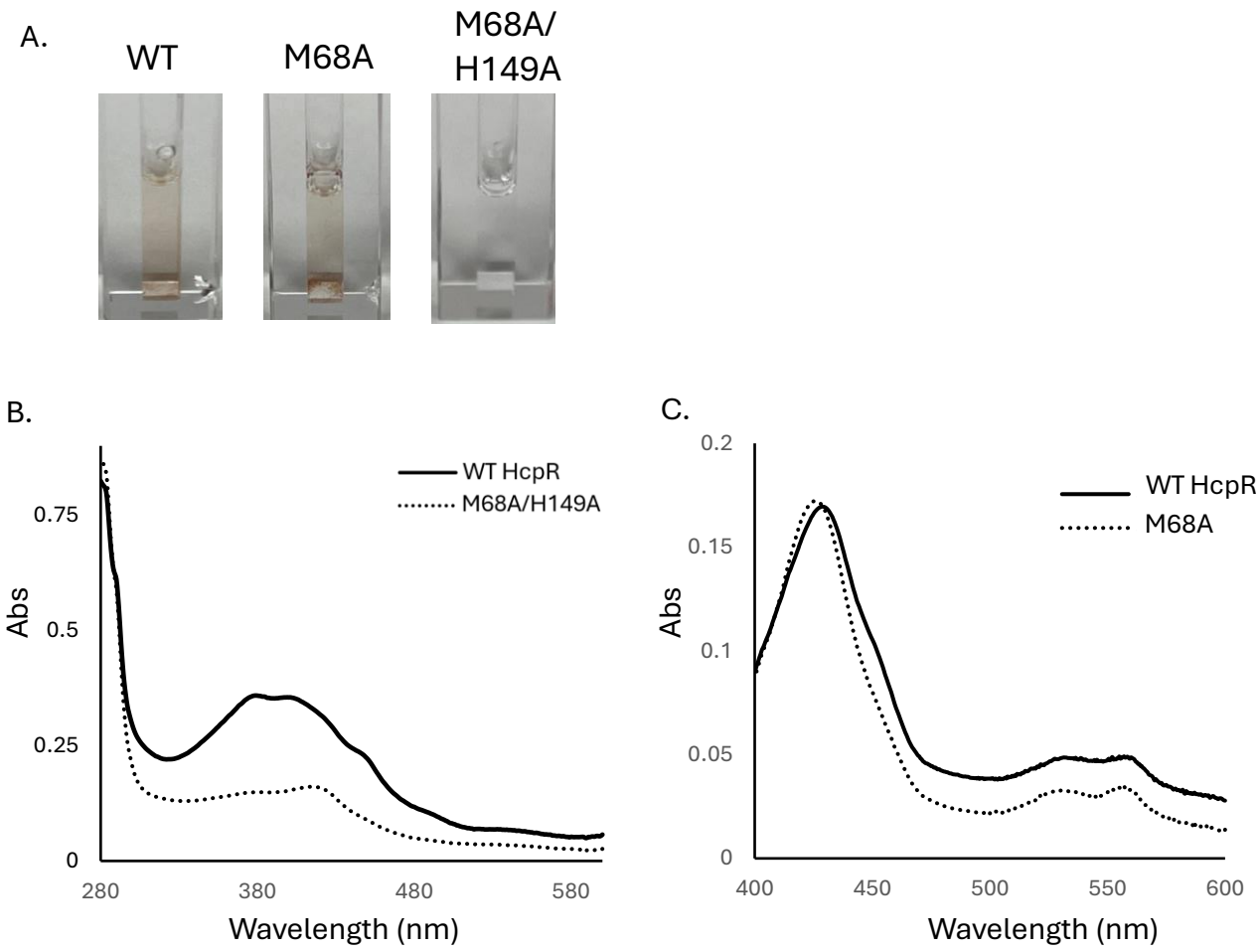
A.
WT
M68A
M68A/
H149A
B.
WT HcpR
M68A/H149A
Abs
0.75
0.5
0.25
0
280
380
480
580
Wavelength (nm)
C.
WT HcpR
M68A
Abs
0.2
0.15
0.1
0.05
0
400
450
500
550
600
Wavelength (nm)
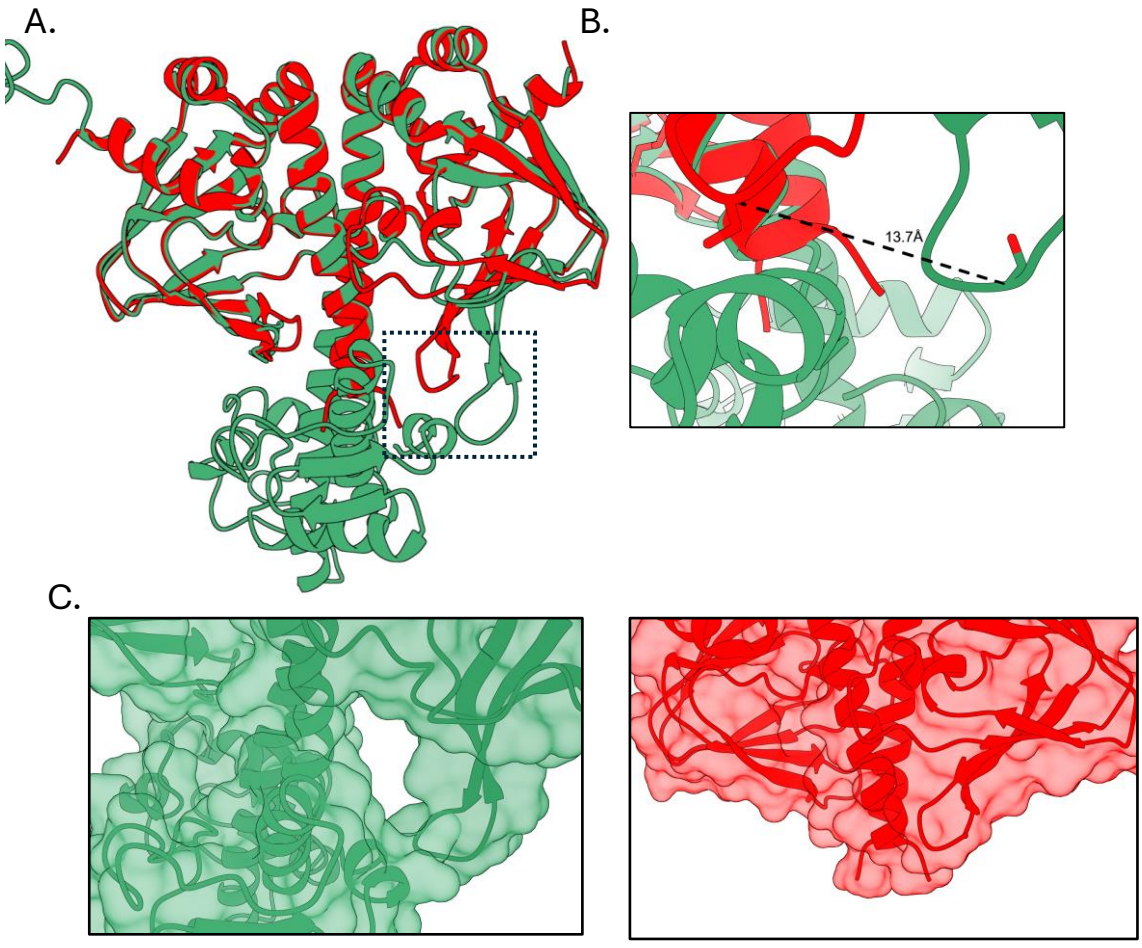
Figure 6